Structure

Article

Structure Determination of the Transactivation Domain of p53 in Complex with S100A4 Using Annexin A2 as a Crystallization Chaperone

Highlights

- p53 TAD forms an asymmetric fuzzy complex with S100A4
- The crystal structure of the complex was solved by utilizing ANXA2
- ANXA2 was found to have better crystal forming ability than wtMBP
- ANXA2 chaperon system can be widely used, but works best with smaller targets

Authors

Péter Ecsédi, Gergő Gógl, Henrietta Hóf, Bence Kiss, Veronika Harmat, László Nyitray

Correspondence

nyitray@elte.hu

In Brief

Ecsédi et al. introduces ANXA2 as a crystallization chaperone with the aim of easing the crystallization of difficult target proteins. As a proof of concept, the crystal structure of the p53 TAD-S100A4 complex is solved by utilizing the crystal forming ability of ANXA2.

Ecsédi et al., 2020, Structure *28*, 1–11
August 4, 2020
https://doi.org/10.1016/j.str.2020.05.001

CellPress

Please cite this article in press as: Ecsédi et al., Structure Determination of the Transactivation Domain of p53 in Complex with S100A4 Using Annexin A2 as a Crystallization Chaperone, Structure (2020), https://doi.org/10.1016/j.str.2020.05.001

Structure

CellPress

Article

Structure Determination of the Transactivation Domain of p53 in Complex with S100A4 Using Annexin A2 as a Crystallization Chaperone

Péter Ecsédi,[1] Gergő Gógl,[1,2] Henrietta Hóf,[1] Bence Kiss,[1] Veronika Harmat,[3] and László Nyitray[1,4,*]
[1]Department of Biochemistry, ELTE Eötvös Loránd University, Budapest 1117, Hungary
[2]Institute of Genetics and of Molecular and Cellular Biology, IGBMC, Strasbourg 67400, France
[3]ELTE Eötvös Loránd University, Institute of Chemistry, MTA-ELTE Protein Modeling Research Group, Budapest 1117, Hungary
[4]Lead Contact
*Correspondence: nyitray@elte.hu
https://doi.org/10.1016/j.str.2020.05.001

SUMMARY

To fully understand the environmental factors that influence crystallization is an enormous task, therefore crystallographers are still forced to work "blindly" trying as many crystallizing conditions and mutations to improve crystal packing as possible. Numerous times these random attempts simply fail even when using state-of-the-art techniques. As an alternative, crystallization chaperones, having good crystal-forming properties, can be invoked. Today, the almost exclusively used such protein is the maltose-binding protein (MBP) and crystallographers need other widely applicable options. Here, we introduce annexin A2 (ANXA2), which has just as good, if not better, crystal-forming ability than the wild-type MBP. Using ANXA2 as heterologous fusion partner, we were able to solve the atomic resolution structure of a challenging crystallization target, the transactivation domain (TAD) of p53 in complex with the metastasis-associated protein S100A4. p53 TAD forms an asymmetric fuzzy complex with the symmetric S1004 and could interfere with its function.

INTRODUCTION

Structural biology methods provide powerful tools to understand protein functions and the underlying mechanisms. Protein crystallography is still the most important technique in this field and, as structure solving methods have become more and more advanced, the production of high-quality diffracting crystals remains the largest challenge for crystallographers. The process of crystallization is affected by numerous factors, including the chemical characteristics of the protein, environmental factors, and conformational heterogeneity (Tereshko et al., 2008). For crystallization, usually a high amount of purified protein is also required. A popular method to facilitate protein expression and purification is using affinity tags, such as His_6-tag (Bornhorst and Falke, 2000), maltose-binding protein (MBP) (Braun et al., 2002), glutathione S-transferase (GST) (Smith, 2000), thioredoxin (TRX) (LaVallie et al., 2000), or several other short peptides or stable proteins fused to the target proteins (Stevens, 2000). Before crystallization, these affinity tags are usually removed using site-specific proteases, which may lead to the precipitation and/or activity loss of the target molecule (Baneyx, 1999). A possible way to avoid these problems and increase the solubility of the target protein is to fuse it to the affinity tag via a short, rigid spacer (lacking any protease cleavage site). This way the conformational heterogeneity of the fusion construct is reduced, which might promote crystallizability and the crystallization ability of the chimeric tag can be exploited (Smyth et al., 2003). In addition, the known structure of the chimeric tag might be used during data processing to facilitate molecular replacement and structural refinement. For this purpose, MBP, GST, and TRX have been used successfully (Waugh, 2016; Jin et al., 2017), together with other well-crystallizing proteins, such as lysozyme (Thorsen et al., 2014; Rosenbaum et al., 2007; Kobilka, 2013) or antibody fragments (Tamura et al., 2019; Lieberman et al., 2011). However, so far only MBP appears to be a generally effective crystallization chaperone and at the same time a useful affinity tag (Waugh, 2016; Clifton et al., 2015), and little effort was made to find alternatives that might be equally or even more adequate for this dual role. The number of structures in the PDB using crystallization chaperones is increasing, indicating that this approach can be a highly efficient tool for crystallographers solving the structures of hardly crystallizable proteins or protein complexes. A good example for such a difficult target, is the complex between the p53 transactivation domain (TAD) and S100A4.

S100A4 is a small, dimeric EF-hand Ca^{2+}-binding protein known by its pathological role in several metastatic tumors and inflammatory diseases (Boye and Maelandsmo, 2010). Its interaction with p53 TAD (1–64) has previously been studied by several groups (Orre et al., 2013; Shen et al., 2015; Grigorian et al., 2001; Fernandez-Fernandez et al., 2008; van Dieck et al., 2010); however, the structure of the complex remains unknown. Note that several other S100 proteins (S100A1, S100A2, S100A4, S100A6, S100A11, and S100B) also bind to p53 TAD

Please cite this article in press as: Ecsédi et al., Structure Determination of the Transactivation Domain of p53 in Complex with S100A4 Using Annexin A2 as a Crystallization Chaperone, Structure (2020), https://doi.org/10.1016/j.str.2020.05.001

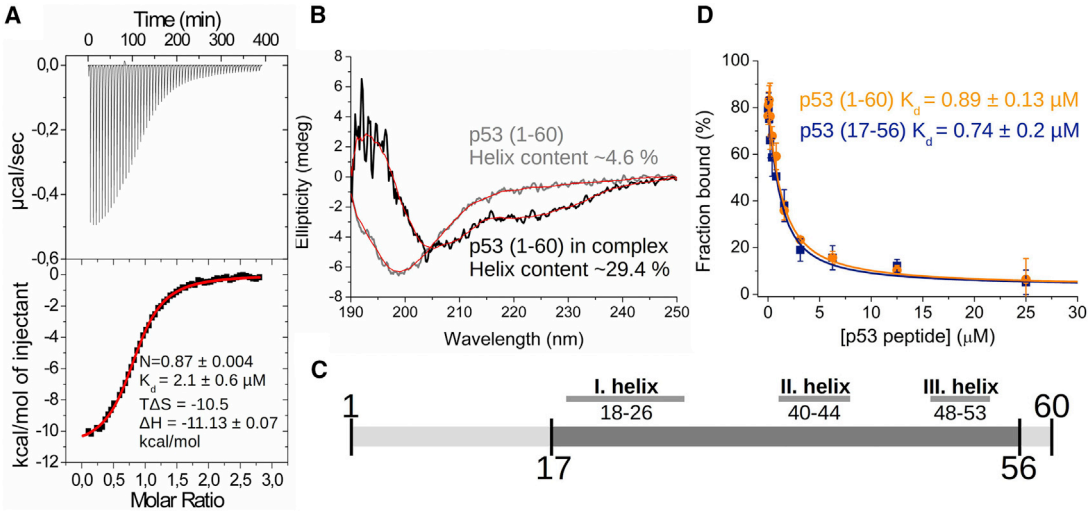

Figure 1. *In Vitro* Characterization of p53 TAD-S100A4 Complex

(A) A 60 µM wild-type S100A4 dimer was titrated with a 500 µM p53 TAD$^{1-60}$ fragment in an isothermal titration calorimetry assay.

(B) CD measurements show that the intrinsically disordered p53 TAD$^{1-60}$ (light gray) adopts a more α-helical structure upon binding to S100A4 (dark gray).

(C) Schematic representation of p53 TAD shows the two fragments that were produced and used in this paper (light and dark gray as p53 TAD$^{1-60}$ and p53 TAD$^{17-56}$, respectively). The three segments with high secondary structure propensity (found by Lee et al., 2000) are highlighted.

(D) Fl-p53 TAD$^{17-56}$ complexed with wild-type S100A4 were titrated with unlabeled p53 TAD$^{1-60}$ and p53 TAD$^{17-56}$ fragments in a fluorescence polarization (FP) assay. Each data point represents the mean ± SD of three independent experiments. Lines represent the fitting of competitive binding equation (Wang, 1995).

(van Dieck et al., 2009b) or to the C-terminal end of p53 containing the tetramerization (TET) (326–356) and the negative regulatory domains (NRD) (364–393) (Fernandez-Fernandez et al., 2005, 2008). S100A4 is a highly soluble protein, even the name S100 refers to the fact that these proteins remain in solution when saturated ammonium sulfate is used (Moore, 1965). This ability makes S100 proteins immensely difficult to crystallize in general, but in the case of p53 the process is even more formidable. In the PDB only NMR structures were published so far containing the whole p53 TAD, which contains both TAD1 and TAD2 subdomains (Harms and Chen, 2006), in complex with a target protein (Yoon et al., 2018; Rowell et al., 2012; Feng et al., 2009; Okuda and Nishimura, 2014; Krauskopf et al., 2018; Krois et al., 2016; Lee et al., 2010). The absence of X-ray structures, including the long TAD, despite the large number of studies, shows that the crystallization of this domain in any protein complex is an inherently difficult task. Remarkably, here using annexin A2 (ANXA2) as a crystallization chaperon we were able to solve the atomic resolution structure of this p53 TAD-S100A4 complex.

ANXA2 is a non-EF-hand Ca^{2+}-binding protein (Gerke and Moss, 2002). Its ability to aggregate ("annex") phospholipid membranes in a Ca^{2+}-dependent manner underlies its biological functions, such as vesicular transport, and exo- and endocytosis (Gerke and Moss, 2002; Drust and Creutz, 1988). ANXA2 consists of a disordered N-terminal (NTD) (2–33) and a highly conserved, rigid C-terminal "core" domains (CTD) (34–339). The convex side of the CTD is responsible for Ca^{2+}-dependent membrane binding while the concave side directs membrane aggregation and anchors the NTD via a highly conserved G-[TS]-[VI] motif localized in the C terminus of the NTD (C-NTD) (23–33) (Ecsédi et al., 2017). ANXA2 is a highly soluble and stable protein and its ability to easily form crystals has recently been observed in our laboratory (Ecsédi et al., 2017). Moreover, beside the case of the p53 TAD-S100A4 complex, studied here, we have already used ANXA2 previously to determine the structure of a PDZ domain with a bound peptide ligand (Gogl et al., 2018). Results presented in this paper suggest that ANXA2 could be another promising crystallization helper molecule similarly to MBP and it is likely applicable to determine the structure of other difficult protein complexes.

RESULTS

In Vitro Characterization of the p53 TAD-S100A4 Complex

A previous NMR study suggested that only parts of TAD1 (residues 17–40) and TAD2 (residues 41–57) are involved in complex formation with S100A4 (van Dieck et al., 2009b). However, several prolines, the contribution of which to the interaction could not be predicted by NMR, are located in N- and C-terminal directions (P^4, P^8, P^{12}, P^{13}, P^{58}, and P^{60}), thus the first 60 residues of p53 was arbitrarily chosen to express as a recombinant peptide (TAD$^{1-60}$) and used in the binding experiments. It was found, using isothermal titration calorimetry measurements, that the interaction between p53 TAD$^{1-60}$ and S100A4 is asymmetric (a single peptide binds to one S100A4 dimer) and its dissociation constant is in the micromolar range (Figure 1A). According to our circular dichroism (CD) measurements, analyzed with the BesStSel secondary structure prediction program (Micsonai et al., 2015), the structure of the originally disordered TAD$^{1-60}$ peptide changes to a more helical structure upon complex formation with S100A4 (α helix content increases from ~4.6% to ~29.4%) (Figure 1B). Note here that by correcting our data with the CD spectrum of the blank buffer ruled out its contribution during the α helix content estimations of peptides.

Please cite this article in press as: Ecsédi et al., Structure Determination of the Transactivation Domain of p53 in Complex with S100A4 Using Annexin A2 as a Crystallization Chaperone, Structure (2020), https://doi.org/10.1016/j.str.2020.05.001

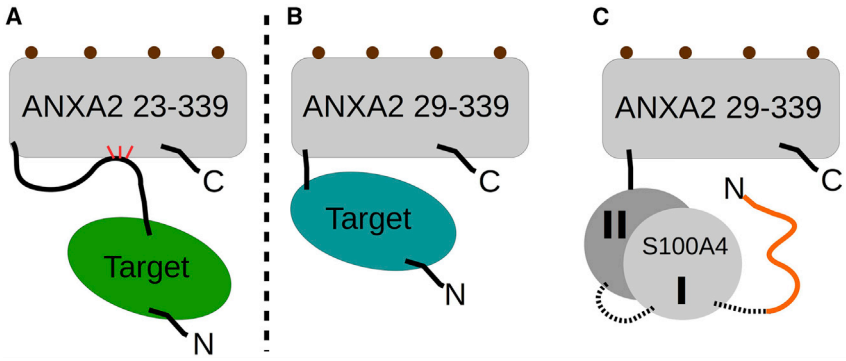

Figure 2. Schematic Representation of the ANXA2 Fusion Constructs Used for the Crystallographic Studies

(A) The target protein is fused to the C-NTD (23–33) of ANXA2. Here the additional interactions between C-NTD and CTD (34–339) (red lines) stabilize the structure of ANXA2.

(B) Almost the whole NTD (2–28) is removed and the target protein is fused directly to the first α helix of ANXA2 core domain (29–339) with a short linker.

(C) In the present work the p53 TAD$^{17-56}$ (orange) was fused to the scS100A4Δ8 (I and II represent the subunits), which is fused to ANXA2$^{29-339}$. Dashed lines indicate the GS linkers. Brown dots represent calcium ions.

A similar effect was observed with other S100 ligands (Fernandez-Fernandez et al., 2008; Kiss et al., 2012). Previously, Lee et al. (2000) have found several regions in the apo p53 TAD peptide with relatively high secondary structure propensity (residues 18–26, 40–44, and 48–53) using NMR spectroscopy (Figure 1C). The number of residues in these transiently formed nascent structural elements are in good agreement with the CD data presented here. Disordered binding regions (IDRs) of proteins usually fold upon binding (Dunker et al., 2001), therefore one can assume that those short-term observed folds of TAD could be key elements in complex formation (Kim and Han, 2018). Nevertheless, the low overall helix propensity of the peptide even in the bound form predicts that TAD probably retains partial flexibility and forms a dynamic, partially folded so-called fuzzy complex (Tompa and Fuxreiter, 2008) with S100A4. These results together with other findings (van Dieck et al., 2009b, 2010) now ensures the previous prediction that the first 16 and the last 8 residues do not participate in the interaction. Therefore, a truncated TAD peptide (residues 17–56, TAD$^{17-56}$) was produced and its binding to S100A4 was evaluated using a competitive fluorescence polarization assay. It revealed that the truncated TAD$^{17-56}$ has the same affinity to S100A4 as the longer TAD$^{1-60}$ peptide (K_d values ~0.7 and ~0.9 μM, respectively) (Figure 1D). Thus the subsequent experiments were conducted using this "minimal" binding sequence of p53 to ease crystallization.

Designing the C-Terminal ANXA2 Fusion Constructs

We have made several attempts to crystallize the p53 TAD$^{17-56}$-S100A4 complex alone or by using GST or wild-type MBP (wtMBP) tags as crystallization chaperones (connected by an "SGSGG" short linker). If either p53 TAD$^{17-56}$ or S100A4 was fused to GST or MBP, respectively, then mixed with the other partner, no crystal was observed in any case. The poor crystal-forming ability of the complex presumably comes from the high solubility of S100A4 and the dynamic, fuzzy binding mode of p53. Following these unavailing attempts, two fusion constructs of ANXA2 were designed, based on its 3D structures (Ecsédi et al., 2017; Gogl et al., 2018), and cloned into a modified pET15 vector together with an N-terminal short multi-cloning site (for inserting the target proteins) followed by a cleavable His_6-tag with the aim of using it as a crystallization chaperone similarly to MBP/GST. One construct (ANXA2$^{23-339}$) contains the so-called C-NTD of ANXA2 that transiently binds to the core domain (Figure 2A). Its presence considerably stabilizes ANXA2 (Ecsédi et al., 2017), thus facilitating crystal formation; however, its structural plasticity may result in a less compact fold with a long disordered linker between the target protein and ANXA2. The other construct (ANXA2$^{29-339}$) does not contain the C-NTD (Figure 2B), which precludes the formation of such a long spacer but results in a less stable core domain (DNA sequences and ANXA2 containing plasmids were uploaded and sent to Addgene with IDs of 136543, 136544, 136545, and 136546).

In a previously published paper, where we have solved the crystal structure of the second PDZ domain of the membrane-associated guanylate kinase (MAGI-1), the former ANXA2 construct was used (Gogl et al., 2018). In the case of p53 TAD$^{17-56}$ we had to apply the latter strategy since S100A4 interacts with the C-NTD of ANXA2 (Ecsédi et al., 2017). To increase the chance of crystal formation, we have produced a chimera where a single-chain S100A4Δ8 dimer (scS100A4Δ8) was fused to ANXA2$^{29-339}$ using the previously designed vectors. In case of scS100A4Δ8 the last eight residues forming a short disordered region, thus presumably negatively affecting crystal formation, were deleted and the two subunits were covalently joined into a single-chain construct (a short linker with the sequence of "SAGSAG" was used between the subunits). Using this chimera, ANXA2 could drive crystal packing instead of the highly soluble S100A4. In our first attempts, where this scS100A4Δ8-ANXA2$^{29-339}$ construct was complexed with p53 TAD$^{17-56}$, the p53 peptide ligand dissociated from the crystals and only the scS100A4Δ8-ANXA2$^{29-339}$ chimera was found in apo form (not deposited in the PDB). We believe that the presence of the fuzzy interaction is unfavorable for crystal formation, thus crystals lacking p53, caused by the temporary dissociation of the peptide, could form more easily causing the elimination of the peptide from its binding site in those structures. To solve this problem we covalently bound p53 TAD$^{17-56}$ to the N terminus of scS100A4Δ8-ANXA2$^{29-339}$ via a GS linker ("GGSG" plus "HM" as cloning artifact) (Figure 2C) to form the ternary chimeric construct of p53 TAD$^{17-56}$-scS100A4Δ8-ANXA2$^{29-339}$. Note here that the artificially produced scS100A4Δ8 allowed the presence of only one covalently bound ANXA2$^{29-339}$ and p53 TAD$^{17-56}$ in the chimera. We have performed model buildings, based on known S100 complexes, to estimate the optimal linker length with the assumption that the flexible residues, located at both the N and C termini of each protein, could act as potential

Please cite this article in press as: Ecsédi et al., Structure Determination of the Transactivation Domain of p53 in Complex with S100A4 Using Annexin A2 as a Crystallization Chaperone, Structure (2020), https://doi.org/10.1016/j.str.2020.05.001

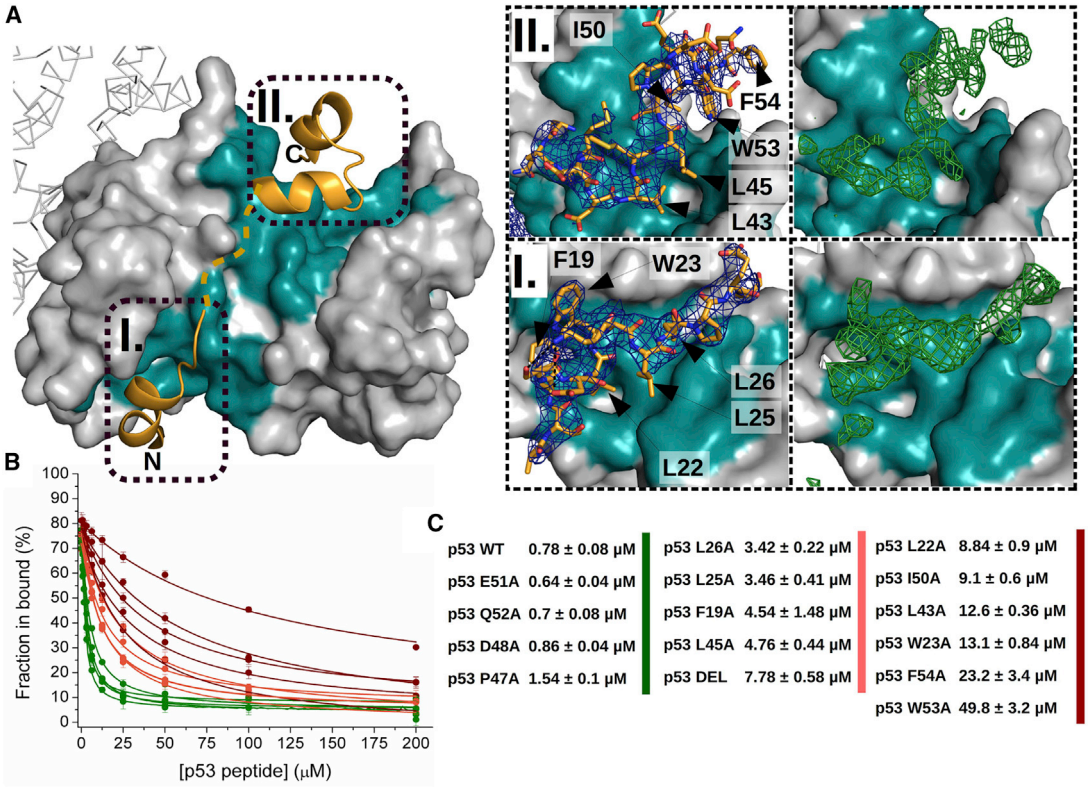

Figure 3. Crystal Structure of p53 TAD$^{17-56}$-scS100A4Δ8 Using ANXA2$^{29-339}$ as Crystallization Chaperone and Its Validation Using Alanine Scanning of p53 TAD

(A) The binding of p53 TAD$^{17-56}$ (bright orange) to scS100A4Δ8 (gray, S100A4 dimer; teal, the interacting surface). ANXA2$^{29-339}$ is visualized here with gray ribbon. The N-terminal (I.) and C-terminal α helices (II.) bind to the hydrophobic pockets of S100A4 (formed by the helices 3, 4, and the hinge region of each subunit), while the region in between (dashed line) makes only transient interactions with the first helices of the dimer. The α helices stabilizing intramolecular interactions of S20 and D21 with K24 of p53 are denoted with black dashed lines. Electron density map of p53 TAD$^{17-56}$ is visualized in blue (final $2F_o - F_c$ contoured at 1.0 sigma) and the $F_o - F_c$ map of a simulated annealing omit map, generated by omitting p53 peptide, is presented in green (contoured at 2.5 sigma).

(B) Fl-p53 TAD$^{17-56}$ complexed with wild-type S100A4 were titrated with unlabeled alanine mutants of p53 TAD$^{17-56}$ in an FP assay. Each data point represents the mean ± SD of three independent experiments. Lines represent the fitting of competitive binding equation (Wang, 1995).

(C) The different p53 TAD mutants are grouped by their relative affinity to wild-type S100A4. Green column, K_d = 1–2 μM; pink column, K_d = 2–8 μM; red column, K_d > 8 μM.

extenders in case the designed linker would turn out to be short and would constrain the interaction itself. Using these optimal linkers the chimeras could be prevented to become overly flexible, which usually hampers crystal formation.

Solving the Crystal Structure of the p53 TAD-S100A4 Complex

Using the p53 TAD$^{17-56}$-scS100A4Δ8-ANXA2$^{29-339}$ construct we could solve the structure of the complex at 3.1 Å resolution (Figure 3A) (Table 1). Two chimeric molecules were found in the asymmetric unit. In both chains, ANXA2$^{29-339}$ was visible, but in chain B the scS100A4Δ8 was presumably very flexible and the electron density map of the complex was very weak. In the case of chain A, however, both scS100A4Δ8 and the p53 fragment could be built into the electron density map. The electron density of the linkers between p53 TAD$^{17-56}$ and scS100A4Δ8, as well as between the S100A4 subunits, were not visible indicating that those additional residues did not affect the binding mode of p53 TAD$^{17-56}$ to scS100A4Δ8. Three short segments of p53 were observed to be in α-helical conformation in the structure. The residues of these observed helices nicely overlap with the residues of the nascent secondary elements and form helices previously found by others in apo (Lee et al., 2000) or in complexed p53 (Lee et al., 2010). The N-terminal α helix (18–25), part of TAD1, makes exclusively hydrophobic interactions (F19, L22, W23, and L25 of p53) with one of the binding pocket of S100A4 dimer. Note that S20/D21 and K24 of p53 form an intramolecular salt bridge stabilizing this α helix. At the C-terminal end of the TAD segment, two more α helices (residues 37–42 and 47–53) are visible in the complex. S37 and S46 N-terminally cap the evolved helices respectively, further stabilizing their structure. Hydrophobic side chains of L43, L45, I50, W53, and F54 of TAD2 appear to be key residues in anchoring this region to S100A4. The large aromatic side chain of W53 nicely fits into the hydrophobic environment formed by F45/F89 of the corresponding subunit and I50/F54 of TAD2, while L43 and L45 of TAD2 face the binding pocket of S100A4. Results of our alanine scanning experiments (Figures 3B and 3C) confirmed the importance of this region. Mutation of I50, W53, or F54 to alanine caused

Please cite this article in press as: Ecsédi et al., Structure Determination of the Transactivation Domain of p53 in Complex with S100A4 Using Annexin A2 as a Crystallization Chaperone, Structure (2020), https://doi.org/10.1016/j.str.2020.05.001

Table 1. Data Collection and Refinement Statistics

	p53 TAD$^{17-56}$-scS100A4Δ8-ANXA2$^{29-339}$
Data Collection	
Space group	P 1 21 1
Cell dimensions	
a, b, c (Å)	95.96, 62.77, 106.02
α, β, γ (°)	90, 90.25, 90
Resolution (Å)[a]	47.98–3.1 (3.18–3.1)
R_{meas} (%)[a]	17.0 (101)
I/σ[a]	10.0 (1.74)
Completeness (%)[a]	99.8 (99.9)
Redundancy[a]	6.68 (5.37)
CC1/2[a]	99.5 (70.1)
Refinement	
Resolution (Å)	47.98–3.1
No. of reflections[a]	155290 (9,136)
R_{work}/R_{free}	0.23/0.272
No. of residues	
Protein	533
Glycerol	2
Ca^{2+}	8
Water	0
B factors	
Protein	73.11
Ca^{2+}	77.4
Glycerol	57.5
Ramachandran plot (%)	
Favored	94
Allowed	6
Outliers	0

Data were collected on single crystals.
[a]Highest-resolution shell is shown in parentheses.

significant decrease in affinity (K_d values increased ~11, ~62, or ~29 times, respectively, compared with the wild-type peptide). Mutation of L22, W23, or L43 caused similar effects (K_d values increased ~11, ~16, or ~16 times, respectively). Matching decrease in affinity was observed by van Dieck et al. (2009b) using L22/Q and W23/S mutants. These data show that p53 TAD anchors to S100A4 mostly by the above residues while other hydrophobic amino acids, namely F19, L25, L26, and L45, further strengthen the interaction (their Ala substitution increases the K_d 4–10 times). Interestingly, the deletion of the middle segment (p53 DEL: residues 31–35, -VLSPL-), which could not be built into the electron density map, hence it might not take part in the interaction with S100A4 despite it containing several hydrophobic residues, decreased the affinity by one order of magnitude. This observation suggests that the middle region of the peptide ligand binds to S100A4 transiently, resulting in the fuzziness of the complex.

Comparing the Crystal-Forming Ability of ANXA2 and wtMBP

To assess the usability of ANXA2 as a crystallization chaperone, we first compared the crystal-forming abilities of wtMBP and ANXA2. For this purpose eight constructs were produced: scS100A4Δ8 and the second PDZ domain of MAGI-1 (PDZ) (previously crystallized, fused to ANXA2 [Gogl et al., 2018]) as target proteins; the crystallization chaperones, wtMBP and ANXA2$^{29-339}$ alone; and the combinations of the target and chaperone proteins (wtMBP-PDZ, wtMBP-scS100A4Δ8, PDZ-ANXA2$^{23-339}$, and scS100A4Δ8-ANXA2$^{29-339}$). Eight-(SSSNNNTS) and 25-residue long (SSSNNNTSGCGGGGGSMSENLYFQG) linker sequences were applied in the case of wtMBP-scS100A4Δ8 and wtMBP-PDZ constructs, respectively. The linkers between wtMBP and target proteins were four residues long in the case of the largest group of reported structures (Jin et al., 2017; Waugh, 2016), although certainly it is also a subject of optimization in our cases; however, several structures were reported using even longer linkers (Waugh, 2016). The PDZ domain represents a smaller (~100 residues) while scS100A4Δ8 a larger (~200 residues) target protein. Using Morpheus and JCSG+ screens we have determined the number of conditions in which each construct gave observable crystals (Figure 4). Based on the results of previous ANXA2 crystallizations, all constructs were used at 250 μM (~8–15 mg/mL for ANXA2$^{29-339}$ and ANXA2 constructs) concentration before mixing, but in the case of wtMBP and wtMBP chimeras the concentration was increased to 2 mM (~82–120 mg/mL) since no crystals were observed during the first screening when lower amount (~10–15 mg/mL) was used. Note here that ANXA2 tend to self-aggregate at high protein concentrations; however at 250 μM we have found no sign of self-association in the absence of phospholipids. In the case of chimeric constructs, the target protein hides the concave side of the CTD, and the NTD is missing, thus they cannot drive the aggregation of ANXA2s as their crucial role in this process was suggested previously (Ecsédi et al., 2017; Lopez-Rodriguez et al., 2018; Lizarbe et al., 2013). Based on these results, we can assume that the chimeric constructs behave differently than ANXA2; therefore, the chimeras might be used even at higher concentrations. Free target proteins could not form crystals at all. WtMBP formed crystals in 14 out of 192 conditions (~7%) while this ratio was ~44% in the case of ANXA2$^{29-339}$ (84/192). This extremely good crystal-forming ability was also observed in the case of PDZ-ANXA2$^{23-339}$ (49/192) (~25%); however, scS100A4Δ8-ANXA2$^{29-339}$ crystallized relatively poorly (9/192) (~4%). The wtMBP chimeras formed no crystals even at the increased concentration. The crystal formation was monitored for a month in all samples; however, no change was observed after a week. To measure the critical concentration of each constructs for crystallogenesis, dilution series of the proteins (using the sample buffer for dilution) were mixed with some of those conditions where crystals were found in the previous experiment (Figure 5). While wtMBP formed crystals only above 500 μM (~20.5 mg/mL) concentration, ANXA2$^{29-339}$ and PDZ-ANXA2$^{23-339}$ could be crystallized at as low concentration as 7 μM (~0.25 and 0.34 mg/mL, respectively). The scS100A4Δ8-ANXA2$^{29-339}$ chimera behaved differently as no crystal growth was observed under 125 μM (~7.5 mg/mL). Note here that other groups previously crystallized MBP at as low concentration as 3.5 mg/mL (Duan et al., 2001). It is also noteworthy however, that we used no mutations in the crystallization chaperone to help crystal formation and in our study only simple screening conditions were tested without any additive or optimization. These might also have improved our MBP results. Overall though, these

Please cite this article in press as: Ecsédi et al., Structure Determination of the Transactivation Domain of p53 in Complex with S100A4 Using Annexin A2 as a Crystallization Chaperone, Structure (2020), https://doi.org/10.1016/j.str.2020.05.001

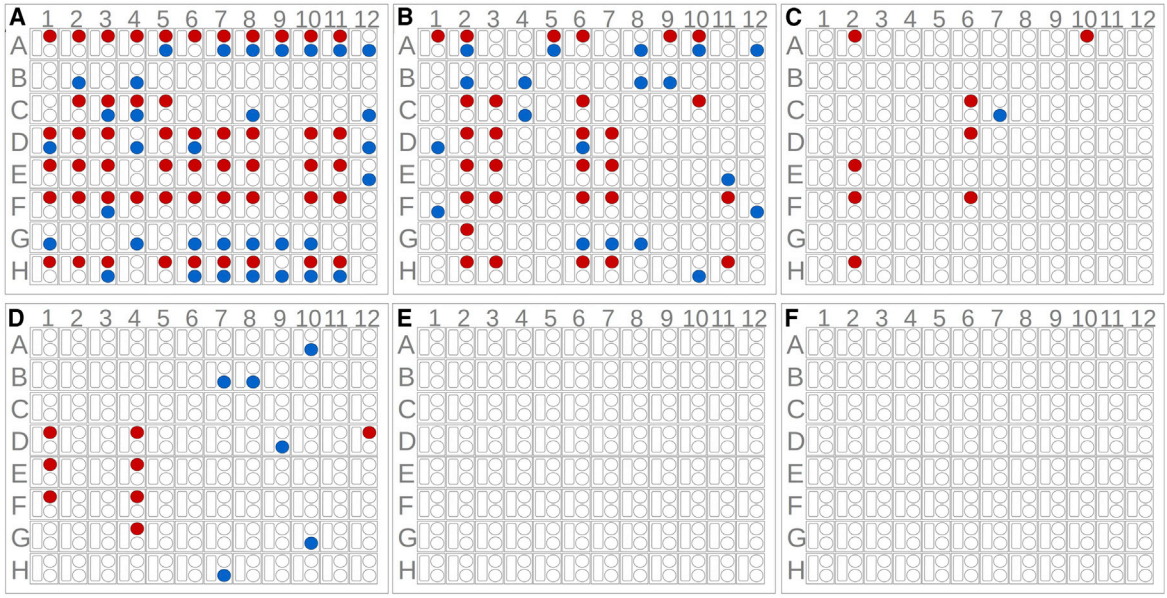

Figure 4. Crystal Screening of Different wtMBP and ANXA2 Constructs

(A and B) (A) ANXA2$^{29-339}$ and (B) PDZ-ANXA2$^{23-339}$ crystals were formed under numerous JCSG+ (blue) and Morpheus (red) crystallization conditions at 250 μM concentration.

(C–F) (C) In the case of the larger scS100A4Δ8-ANXA2$^{29-339}$ construct, crystal formation significantly dropped. Crystal formation of (D) wtMBP, (E) wtMBP-PDZ, and (F) wtMBP-scS100A4Δ8 at 2 mM concentration is also presented. Crystal growth was monitored for a month.

experiments provide a proof-of-concept that ANXA2 is a very good candidate to use as a crystallization chaperon.

DISCUSSION

Crystallization of proteins is currently still attempted by brute force, screening a tremendous amount of conditions (McPherson and Cudney, 2014), or by designing scores of mutations (Cooper et al., 2007; Gogl et al., 2013). As an alternative, recombinant crystallization chaperones such as the most commonly used MBP can be complexed or even fused to the target protein. However, alone this MBP fusion system cannot fulfill the needs of crystallographers as this system has its own limitations (Holcomb et al., 2017). Thus, exploring novel or even better crystallization chaperones might help to bypass the main bottleneck of crystallography, namely the production of well diffracting crystals. We show here that ANXA2, a Ca^{2+} and membrane binding protein might be the next candidate for this purpose. Naturally, predicting the applicability of this new chaperon system, at least for the time being, is very difficult since only a few crystallization trials were made. However, our data show some promising results, namely that ANXA2 has a better crystallizing ability compared with the still very effective wtMBP and it is also a highly soluble protein with a compact and stable structure. Moreover, ANXA2 can also be used as a purification tag owing to its calcium-dependent heparin binding activity, a property shared only by a few other proteins, such as serum amyloid P component, P- and L-selectins, and ANXA5 (Capila and Linhardt, 2002; Shao et al., 2006). Utilizing this ability of ANXA2, a heparin column can be used for a specific affinity-based purification (Shao et al., 2006; Gokhale et al., 2005; Hubaishy et al., 1995) easing the production of highly purified samples for crystallography.

To further explore this approach, we purified the scS100A4Δ8-ANXA229-339 construct using Ni^{2+} and heparin affinity chromatography (Figure S1). ANXA2 and thus likely other ANXA2-based chimeras can also be specifically purified using only anion and cation exchange columns, omitting affinity chromatography as described previously (Ecsédi et al., 2017).

Crystal Packing and the Limitation of the ANXA2 Chaperone System

To understand the remarkable crystal-forming ability of ANXA2, several ANXA2 structures in the PDB were analyzed (Figures 6 and 7). It appears that ANXA2 forms one type of crystal packing interaction in most cases. In the crystals, ANXA2 molecules build a spiral-like structure with a Ca^{2+} partially coordinated by the carbonyl groups of M278, G280, and G282, and the carboxyl group of D322 from one molecule (molecule A) (Figure 7) and partially by the carboxyl group of S234 of another ANXA2 (molecule B). Note that ANXA2 could form crystals differently depending on its partner (Figure 6E). Interestingly, this type of coordination of Ca^{2+} in the crystal exists mostly in the case of ANXA2 structures in the family. ANXA1 (Rosengarth and Luecke, 2003) (PDB: 1MCX) and bovine ANXA6 (Avila-Sakar et al., 1998) (PDB: 1AVC) are exceptions where D196 and 237D of molecule B complete the number of coordinating residues of molecule A. Other contacts further strengthen this intermolecular interaction. Residues of E189 (B), D192 (B), R196 (B), K312 (A), Y317 (A), and Q321 (A) form a chain of salt bridges, while Y188 (B) and Y311 (A) make stacking interactions (Figure 7). Importantly, the crystal packing of ANXA2 is not tight and large solution channels appear between molecules. Analyzing the structures of PDZ-ANXA2$^{23-339}$ (Gogl et al., 2018) and p53 TAD$^{17-56}$-scS100A4Δ8-ANXA2$^{29-339}$ chimeras, the difference is clearly

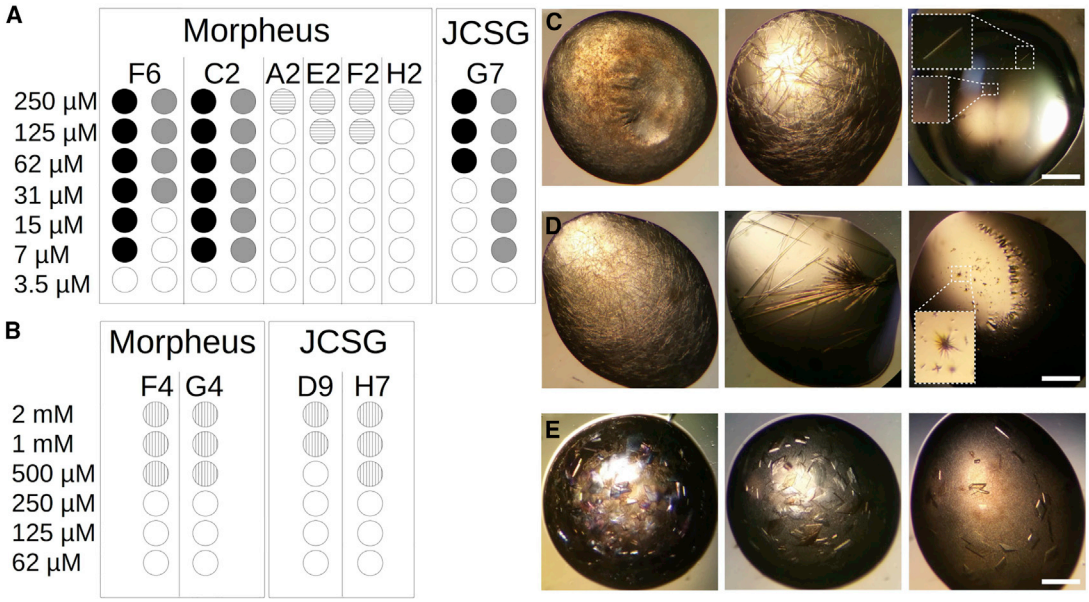

Figure 5. Crystallization of ANXA2 Constructs and wtMBP at Different Concentrations Using the Best Conditions Found in the Screening Experiments

Formation of (A) ANXA2$^{29-339}$ (black), PDZ-ANXA2$^{23-339}$ (gray), and scS100A4Δ8-ANXA2$^{29-339}$ (horizontal lines) crystals were monitored at different protein concentrations for a month.

(B) MBP crystals (vertical lines) formed only at higher than 500 μM concentration (~20.5 mg/mL). No MBP fused constructs were tested since no hit was found during screening.

(C–E) (C) PDZ-ANXA2$^{23-339}$, (D) ANXA2$^{29-339}$, and (E) wtMBP crystals when samples were used at 250 μM (2 mM), 62.5 μM (1 mM), and 7 μM concentrations (0.5 mM) from left to right (wtMBP concentrations are in parenthesis). Small crystals are highlighted in white boxes. White bars represent 0.5 mm.

visible. The PDZ domain (~100 residues) can easily fit into these channels but the scS100A4Δ8 (~200 residues) is too large and must find an alternative position (Figure 6), which hampers crystal formation but still does not inhibit it entirely as was observed in the screening experiments. This comparison of PDZ and scS100A4Δ8 chimeras shows some limitation of this system, namely the size of the target protein. We should note here that the need for reliable methods for crystallization of small target proteins is not fading but increasing in the era of cryoelectron microscopy (cryo-EM). In this size range, although using NMR is also an option, crystallography is still and will be the best experimental method. Numerous difficult, but small target proteins or isolated domains, components of large complexes, which can even be later used in refinements of cryo-EM models, are in the optimal size range for the ANXA2 chaperon system.

If the target molecules are too large or the crystals diffract poorly, other strategies are worth considering. In the case of protein-peptide complexes, instead of the target protein, the target peptide can be fused to ANXA2 and the peptide-ANXA2 construct should be complexed with the partner protein. Another possible strategy is to fuse the target protein to ANXA2 without any flexible linker in a way where the last helix of the target is continuous with the first helix of ANXA2. A similar modification was suggested and used by Jin et al. (2017) producing an MBP-IPS-1 CARD construct. It decreased the mobility of the target protein and improved the quality of their diffraction data. Moreover, similarly to MBP (Moon et al., 2010), some specific modifications in the sequence of ANXA2 might further increase its crystal-forming ability or the sizes of solution channels. One possible way could be to exchange S234 (B molecule) to D/E234 and in parallel mutate D322 (A molecule) to serine to increase the Ca^{2+} co-coordinating effect of molecule B.

Structure of the Fuzzy p53 TAD-S100A4 Complex Determined with ANXA2 as Crystallization Chaperone

In a structural viewpoint, as mentioned above, no X-ray structure, containing both TAD1 and TAD2 subdomains of p53, was available in the PDB previously, showing how challenging a crystallization target TAD is. In this work, using ANXA2 as a crystallization chaperone, we could solve the first such structure of p53 TAD in complex with S100A4. The new structure reveals that nearly the whole p53 TAD binds asymmetrically to the S100A4 dimer similarly to non-muscle myosin 2 A (Kiss et al., 2012) and ANXA2 (Ecsédi et al., 2017). The intrinsically disordered TAD forms three short helices upon interacting with S100A4. Interestingly, these α helices are remarkably similar to other TAD complexes determined by NMR spectroscopy, such as p53-p300 (Feng et al., 2009), p73-MDM2 (Shin et al., 2015), p53-HMG-box (Rowell et al., 2012), and identical to the helices found in the p53-CBP complex (Lee et al., 2010). This highlights the versatility of p53 TAD and explains the observed transient fuzzy binding mode, since it must form interactions with a large number of partners. Previously, the middle helix (residues 37–42) was observed only in the structures of p53-CBP and p53-RPA70 complexes (Bochkareva et al., 2005). The structure of p53-S100A4 further supports that this middle helix might be a more general feature as a third binding region, beside the general TAD1 (18–25) and TAD2 (47–53) sites, increasing the number of

Please cite this article in press as: Ecsédi et al., Structure Determination of the Transactivation Domain of p53 in Complex with S100A4 Using Annexin A2 as a Crystallization Chaperone, Structure (2020), https://doi.org/10.1016/j.str.2020.05.001

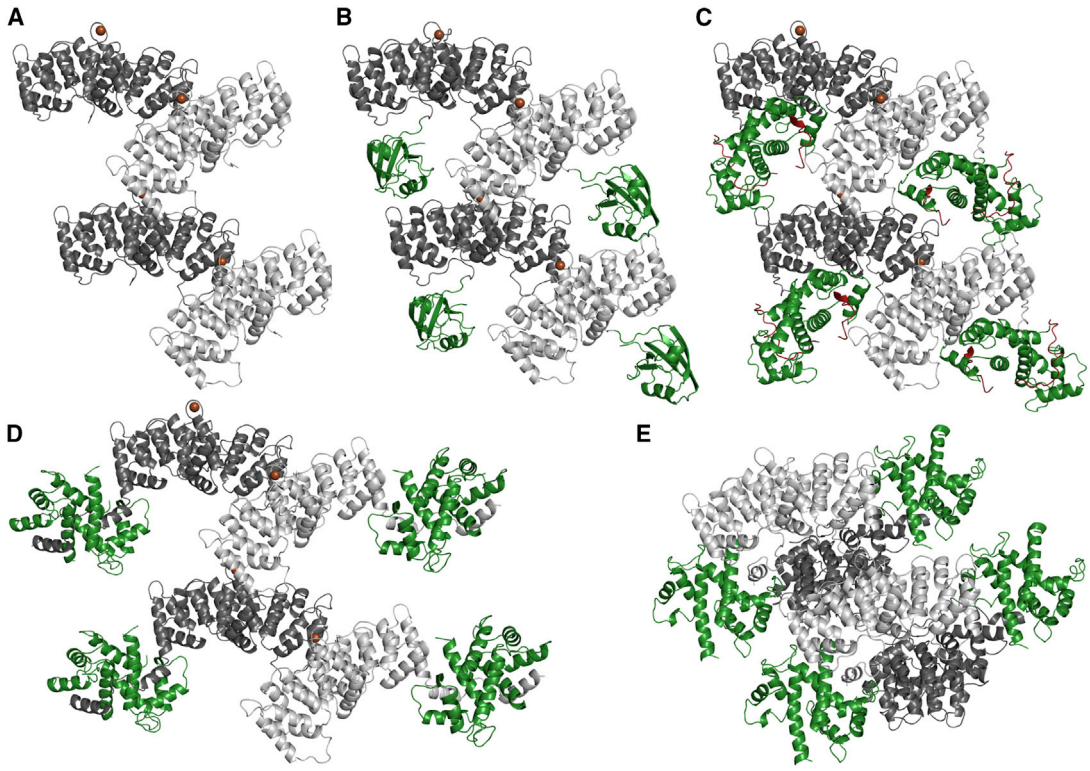

Figure 6. Crystal Packing of ANXA2 in Structures Found in the PDB

(A–C) (A) ANXA2 in Ca^{2+}-bound form (PDB: 1XJL, light and dark gray) (Rosengarth and Luecke, 2004) produces elongated crystal lattices (same in PDB: 5LPX, 5LQ0, 2HYW, 4X9P, and 5LQ2 structures) (Ecsédi et al., 2017; Shao et al., 2006; Raddum et al., 2015). Structures of previously solved (B) PDZ-ANXA2$^{23-339}$ (PDB: 5N7D, PDZ in green) (Gogl et al., 2018), (C) p53 TAD$^{17-56}$-scS100A4Δ8-ANXA2$^{29-339}$ (PDB: 6T58; p53 TAD$^{17-56}$ in red and scS100A4Δ8 in green) chimeras, and the (D) S100A4-ANXA2 complex (PDB: 5LPU, S100A4 in green) (Ecsédi et al., 2017) keeps this crystal packing mode.

(D) In the case of the native, non-fused S100A4-ANXA2 complex, the S100A4 dimer leaves the ANXA2-formed pockets and localizes beside the molecules.

(E) S100A10 binds ANXA2 in a Ca^{2+}-independent manner (PDB: 4HRE) (Oh et al., 2013). Here the observed crystal contacts do not form. S100A10 binds two ANXA2 proteins allowing the formation of a different crystal packing mode.

potential binding modes of p53 TAD. Note that it would be interesting to solve the above structures using X-ray with full-length TAD peptide and compare them with previous NMR data. Based on our results, ANXA2 could be an ideal chaperone for successful crystallization of these other fuzzy complexes.

One might ask whether, in the crystal structure of the chimeric complex, the S100 target and the TAD peptide interacts the same way as in native conditions. By applying a combination of NMR spectroscopy and MD simulations, using full-length p53 TAD and S100A4, we have built a model that is very similar to the chimeric crystal structure, thus confirming our results. It displays a fuzzy complex with three helices overlapping with those in the crystal structure (unpublished data).

From the biological side, the exact function and cancer-promoting effect of the p53 TAD-S100A4 complex is not yet clear (Orre et al., 2013; Grigorian et al., 2001). TAD has moderate affinity toward S100A4 and the interacting surfaces in TAD1 and TAD2 overlap with the binding sites of known physiological p53 partners, such as MDM2, p300, or CRAB (Rajagopalan et al., 2010; Kussie et al., 1996; Raj and Attardi, 2017). These observations suggest that TAD is presumably bound to other partner proteins than S100A4. Nevertheless, in various metastatic tumors S100A4 concentrations were found to be increased by several orders of magnitude (Bresnick et al., 2015; Fei et al., 2017). This increase in expression levels and several posttranslational modifications on p53 TAD (van Dieck et al., 2009b) might be sufficient for the p53-S100A4 fuzzy complex to form, despite the presence of the more physiological negative regulators or co-activators. In that case, similarly to overexpression of MDM2 or TAD mutations, S100A4 could sequester p53, leading to the loss of tumor suppressor function of p53 (Orre et al., 2013). A recent study also showed that p53 TAD2 and PRR subdomains are important for regulating DNA binding of p53 via interacting with its DBD (He et al., 2019). Since S100A4 binds p53 TAD2, the DNA recognition of p53 might be also disrupted trapping the protein in non-specific regions of the genome, interfering with DNA damage detection. Moreover, another group suggested that S100A4 and different S100A4-related members of the family might have a dual role in regulating p53 by promoting and inhibiting its function depending on cell conditions (van Dieck et al., 2009a). As one can see, the function of this cancer- and metastasis-related p53 TAD-S100A4 complex (Fei et al., 2017; Orre et al., 2013; Shen et al., 2015) is yet unclear; however, the detailed study and structure presented here could facilitate further research aiming to study the potential functions of this interaction.

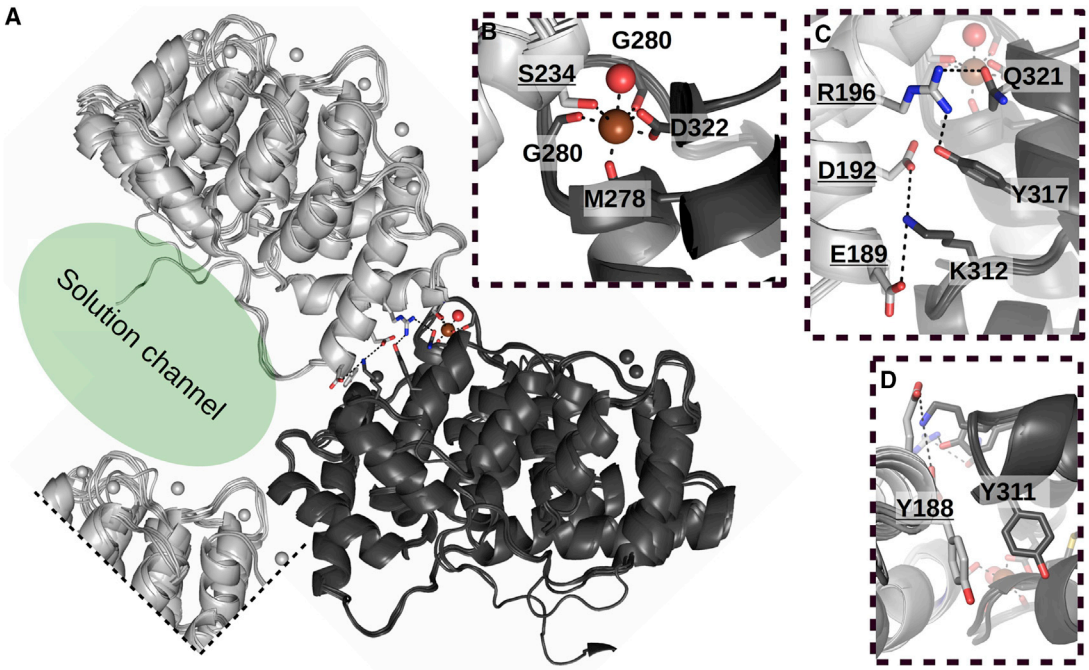

Figure 7. Crystal Contacts of Two ANXA2 Molecules

(A) The aligned ANXA2 structures (PDB: 5LPX, 5LQ0, 5LPU, 1XJL, 2HYW, 4X9P, and 5LQ2) (Ecsédi et al., 2017; Rosengarth and Luecke, 2004; Raddum et al., 2015; Shao et al., 2006) show the conservative crystal contacts. The additional segments of the crystal lattice (light gray ANXA2s are in identical position) defines the solution channel (green ellipse) formed in ANXA2 crystals.

(B) S234 of light gray (molecule B) ANXA2 helps the coordination of Ca^{2+} (brown sphere) connecting to dark gray ANXA2 (molecule A).

(C and D) (C) Besides Ca^{2+} coordination, residues of the nearby α helices form ionic, while (D) two tyrosines form hydrophobic interactions, further stabilizing the assembly. Residues of molecule B are underlined.

STAR★METHODS

Detailed methods are provided in the online version of this paper and include the following:

- KEY RESOURCES TABLE
- RESOURCE AVAILABILITY
  - Lead Contact
  - Materials Availability
  - Data and Code Availability
- EXPERIMENTAL MODEL AND SUBJECT DETAILS
  - E. coli BL21(DE) Cells (NEB)
  - E.coli DH5α Cells (NEB)
- METHOD DETAILS
  - Cloning, Protein Expression and Purification
  - Fluorescent Labeling
  - Crystallization, Data Collection and Structure Determination
  - Crystal Screening of Chimera Constructs
  - Isothermal Titration Calorimetry (ITC)
  - Circular Dichroism (CD) Spectrometry
  - Fluorescence Polarization (FP) Measurements
- QUANTIFICATION AND STATISTICAL ANALYSIS

SUPPLEMENTAL INFORMATION

Supplemental Information can be found online at https://doi.org/10.1016/j.str.2020.05.001.

ACKNOWLEDGMENT

We thank the staff members at the beamlines PXIII of SLS for assistance in data collection. This work was supported by the National Research Development and Innovation Fund of Hungary (K 119359 to L.N.). Project no. 2018-1.2.1-NKP-2018-00005 has been implemented with the support provided from the National Research Development and Innovation Fund of Hungary, financed under the 2018-1.2.1-NKP funding scheme. This work was also supported by projects nos. VEKOP-2.3.2-16-2017-00014 and VEKOP-2.3.3-15-2017-00018 was supported by the European Union and the State of Hungary, co-financed by the European Regional Development Fund. This work was completed in the ELTE Institutional Excellence Program supported by the National Research Development and Innovation Office (NKFIH-1157-8/2019-DT) as well as in the ELTE Thematic Excellence Programme supported by the Hungarian Ministry for Innovation and Technology. G.G. was supported by the Post-doctorants en France program of the Fondation ARC.

AUTHOR CONTRIBUTIONS

P.E., G.G., H.H., and B.K. designed and performed the research. P.E., G.G., and B.K. analyzed the data. P.E., G.G., V.H., and L.N. wrote the paper, L.N. oversaw the research.

DECLARATION OF INTERESTS

The authors declare no conflict of interest.

Received: November 26, 2019
Revised: April 5, 2020
Accepted: May 1, 2020
Published: May 21, 2020

REFERENCES

Adams, P.D., Afonine, P.V., Bunkoczi, G., Chen, V.B., Davis, I.W., Echols, N., Headd, J.J., Hung, L.W., Kapral, G.J., Grosse-Kunstleve, R.W., et al. (2010). PHENIX: a comprehensive Python-based system for macromolecular structure solution. Acta Crystallogr. D Biol. Crystallogr. *66*, 213–221.

Avila-Sakar, A.J., Creutz, C.E., and Kretsinger, R.H. (1998). Crystal structure of bovine annexin VI in a calcium-bound state. Biochim. Biophys. Acta *1387*, 103–116.

Baneyx, F. (1999). Recombinant protein expression in *Escherichia coli*. Curr. Opin. Biotechnol. *10*, 411–421.

van den Berg, S., Lofdahl, P.A., Hard, T., and Berglund, H. (2006). Improved solubility of TEV protease by directed evolution. J. Biotechnol. *121*, 291–298.

Bochkareva, E., Kaustov, L., Ayed, A., Yi, G.S., Lu, Y., Pineda-Lucena, A., Liao, J.C., Okorokov, A.L., Milner, J., Arrowsmith, C.H., and Bochkarev, A. (2005). Single-stranded DNA mimicry in the p53 transactivation domain interaction with replication protein A. Proc. Natl. Acad. Sci. U S A *102*, 15412–15417.

Bornhorst, J.A., and Falke, J.J. (2000). Purification of proteins using polyhistidine affinity tags. Methods Enzymol. *326*, 245–254.

Boye, K., and Maelandsmo, G.M. (2010). S100A4 and metastasis: a small actor playing many roles. Am. J. Pathol. *176*, 528–535.

Braun, P., Hu, Y., Shen, B., Halleck, A., Koundinya, M., Harlow, E., and Labaer, J. (2002). Proteome-scale purification of human proteins from bacteria. Proc. Natl. Acad. Sci. U S A *99*, 2654–2659.

Bresnick, A.R., Weber, D.J., and Zimmer, D.B. (2015). S100 proteins in cancer. Nat. Rev. Cancer *15*, 96–109.

Capila, I., and Linhardt, R.J. (2002). Heparin-protein interactions. Angew. Chem. Int. Ed. *41*, 391–412.

Clifton, M.C., Dranow, D.M., Leed, A., Fulroth, B., Fairman, J.W., Abendroth, J., Atkins, K.A., Wallace, E., Fan, D., Xu, G., et al. (2015). A maltose-binding protein fusion construct yields a robust crystallography platform for MCL1. PLoS One *10*, e0125010.

Cooper, D.R., Boczek, T., Grelewska, K., Pinkowska, M., Sikorska, M., Zawadzki, M., and Derewenda, Z. (2007). Protein crystallization by surface entropy reduction: optimization of the SER strategy. Acta Crystallogr. D Biol. Crystallogr. *63*, 636–645.

van Dieck, J., Fernandez-Fernandez, M.R., Veprintsev, D.B., and Fersht, A.R. (2009a). Modulation of the oligomerization state of p53 by differential binding of proteins of the S100 family to p53 monomers and tetramers. J. Biol. Chem. *284*, 13804–13811.

van Dieck, J., Teufel, D.P., Jaulent, A.M., Fernandez-Fernandez, M.R., Rutherford, T.J., Wyslouch-Cieszynska, A., and Fersht, A.R. (2009b). Posttranslational modifications affect the interaction of S100 proteins with tumor suppressor p53. J. Mol. Biol. *394*, 922–930.

van Dieck, J., Brandt, T., Teufel, D.P., Veprintsev, D.B., Joerger, A.C., and Fersht, A.R. (2010). Molecular basis of S100 proteins interacting with the p53 homologs p63 and p73. Oncogene *29*, 2024–2035.

Drust, D.S., and Creutz, C.E. (1988). Aggregation of chromaffin granules by calpactin at micromolar levels of calcium. Nature *331*, 88–91.

Duan, X., Hall, J.A., Nikaido, H., and Quiocho, F.A. (2001). Crystal structures of the maltodextrin/maltose-binding protein complexed with reduced oligosaccharides: flexibility of tertiary structure and ligand binding. J. Mol. Biol. *306*, 1115–1126.

Dunker, A.K., Lawson, J.D., Brown, C.J., Williams, R.M., Romero, P., Oh, J.S., Oldfield, C.J., Campen, A.M., Ratliff, C.M., Hipps, K.W., et al. (2001). Intrinsically disordered protein. J. Mol. Graph Model. *19*, 26–59.

Ecsédi, P., Kiss, B., Gogl, G., Radnai, L., Buday, L., Koprivanacz, K., Liliom, K., Leveles, I., Vertessy, B., Jeszenoi, N., et al. (2017). Regulation of the equilibrium between closed and open conformations of annexin A2 by N-terminal phosphorylation and S100A4-binding. Structure *25*, 1195–1207.e5.

Emsley, P., Lohkamp, B., Scott, W.G., and Cowtan, K. (2010). Features and development of Coot. Acta Crystallogr. D Biol. Crystallogr. *66*, 486–501.

Fei, F., Qu, J., Zhang, M., Li, Y., and Zhang, S. (2017). S100A4 in cancer progression and metastasis: a systematic review. Oncotarget *8*, 73219–73239.

Feng, H., Jenkins, L.M., Durell, S.R., Hayashi, R., Mazur, S.J., Cherry, S., Tropea, J.E., Miller, M., Wlodawer, A., Appella, E., and Bai, Y. (2009). Structural basis for p300 Taz2-p53 TAD1 binding and modulation by phosphorylation. Structure *17*, 202–210.

Fernandez-Fernandez, M.R., Veprintsev, D.B., and Fersht, A.R. (2005). Proteins of the S100 family regulate the oligomerization of p53 tumor suppressor. Proc. Natl. Acad. Sci. U S A *102*, 4735–4740.

Fernandez-Fernandez, M.R., Rutherford, T.J., and Fersht, A.R. (2008). Members of the S100 family bind p53 in two distinct ways. Protein Sci. *17*, 1663–1670.

Gerke, V., and Moss, S.E. (2002). Annexins: from structure to function. Physiol. Rev. *82*, 331–371.

Gingras, A.R., Basran, J., Prescott, A., Kriajevska, M., Bagshaw, C.R., and Barsukov, I.L. (2008). Crystal structure of the Ca(2+)-form and Ca(2+)-binding kinetics of metastasis-associated protein, S100A4. FEBS Lett. *582*, 1651–1656.

Gogl, G., Toro, I., and Remenyi, A. (2013). Protein-peptide complex crystallization: a case study on the ERK2 mitogen-activated protein kinase. Acta Crystallogr. D Biol. Crystallogr. *69*, 486–489.

Gogl, G., Biri-Kovacs, B., Poti, A.L., Vadaszi, H., Szeder, B., Bodor, A., Schlosser, G., Acs, A., Turiak, L., Buday, L., et al. (2018). Dynamic control of RSK complexes by phosphoswitch-based regulation. FEBS J. *285*, 46–71.

Gokhale, N.A., Abraham, A., Digman, M.A., Gratton, E., and Cho, W. (2005). Phosphoinositide specificity of and mechanism of lipid domain formation by annexin A2-p11 heterotetramer. J. Biol. Chem. *280*, 42831–42840.

Grigorian, M., Andresen, S., Tulchinsky, E., Kriajevska, M., Carlberg, C., Kruse, C., Cohn, M., Ambartsumian, N., Christensen, A., Selivanova, G., and Lukanidin, E. (2001). Tumor suppressor p53 protein is a new target for the metastasis-associated Mts1/S100A4 protein: functional consequences of their interaction. J. Biol. Chem. *276*, 22699–22708.

Harms, K.L., and Chen, X. (2006). The functional domains in p53 family proteins exhibit both common and distinct properties. Cell Death Differ. *13*, 890–897.

He, F., Borcherds, W., Song, T., Wei, X., Das, M., Chen, L., Daughdrill, G.W., and Chen, J. (2019). Interaction between p53 N terminus and core domain regulates specific and nonspecific DNA binding. Proc. Natl. Acad. Sci. U S A *116*, 8859–8868.

Holcomb, J., Spellmon, N., Zhang, Y., Doughan, M., Li, C., and Yang, Z. (2017). Protein crystallization: eluding the bottleneck of X-ray crystallography. AIMS Biophys. *4*, 557–575.

Hubaishy, I., Jones, P.G., Bjorge, J., Bellagamba, C., Fitzpatrick, S., Fujita, D.J., and Waisman, D.M. (1995). Modulation of annexin II tetramer by tyrosine phosphorylation. Biochemistry *34*, 14527–14534.

Jin, T., Chuenchor, W., Jiang, J., Cheng, J., Li, Y., Fang, K., Huang, M., Smith, P., and Xiao, T.S. (2017). Design of an expression system to enhance MBP-mediated crystallization. Sci. Rep. *7*, 40991.

Kabsch, W. (2010). Xds. Acta Crystallogr. D Biol. Crystallogr. *66*, 125–132.

Kim, D.H., and Han, K.H. (2018). Transient secondary structures as general target-binding motifs in intrinsically disordered proteins. Int. J. Mol. Sci. *19*, https://doi.org/10.3390/ijms19113614.

Kiss, B., Duelli, A., Radnai, L., Kekesi, K.A., Katona, G., and Nyitray, L. (2012). Crystal structure of the S100A4-nonmuscle myosin IIA tail fragment complex reveals an asymmetric target binding mechanism. Proc. Natl. Acad. Sci. U S A *109*, 6048–6053.

Kobilka, B. (2013). The structural basis of G-protein-coupled receptor signaling (Nobel Lecture). Angew. Chem. Int. Ed. *52*, 6380–6388.

Krauskopf, K., Gebel, J., Kazemi, S., Tuppi, M., Lohr, F., Schafer, B., Koch, J., Guntert, P., Dotsch, V., and Kehrloesser, S. (2018). Regulation of the activity in the p53 family depends on the organization of the transactivation domain. Structure *26*, 1091–1100.e4.

Krois, A.S., Ferreon, J.C., Martinez-Yamout, M.A., Dyson, H.J., and Wright, P.E. (2016). Recognition of the disordered p53 transactivation domain by the transcriptional adapter zinc finger domains of CREB-binding protein. Proc. Natl. Acad. Sci. U S A *113*, E1853–E1862.

Kussie, P.H., Gorina, S., Marechal, V., Elenbaas, B., Moreau, J., Levine, A.J., and Pavletich, N.P. (1996). Structure of the MDM2 oncoprotein bound to the p53 tumor suppressor transactivation domain. Science *274*, 948–953.

LaVallie, E.R., Lu, Z., Diblasio-Smith, E.A., Collins-Racie, L.A., and McCoy, J.M. (2000). Thioredoxin as a fusion partner for production of soluble recombinant proteins in *Escherichia coli*. Methods Enzymol. *326*, 322–340.

Lee, H., Mok, K.H., Muhandiram, R., Park, K.H., Suk, J.E., Kim, D.H., Chang, J., Sung, Y.C., Choi, K.Y., and Han, K.H. (2000). Local structural elements in the mostly unstructured transcriptional activation domain of human p53. J. Biol. Chem. *275*, 29426–29432.

Lee, C.W., Martinez-Yamout, M.A., Dyson, H.J., and Wright, P.E. (2010). Structure of the p53 transactivation domain in complex with the nuclear receptor coactivator binding domain of CREB binding protein. Biochemistry *49*, 9964–9971.

Lieberman, R.L., Culver, J.A., Entzminger, K.C., Pai, J.C., and Maynard, J.A. (2011). Crystallization chaperone strategies for membrane proteins. Methods *55*, 293–302.

Lizarbe, M.A., Barrasa, J.I., Olmo, N., Gavilanes, F., and Turnay, J. (2013). Annexin-phospholipid interactions. Functional implications. Int. J. Mol. Sci. *14*, 2652–2683.

Lopez-Rodriguez, J.C., Martinez-Carmona, F.J., Rodriguez-Crespo, I., Lizarbe, M.A., and Turnay, J. (2018). Molecular dissection of the membrane aggregation mechanisms induced by monomeric annexin A2. Biochim. Biophys. Acta Mol. Cell Res. *1865*, 863–873.

McCoy, A.J. (2007). Solving structures of protein complexes by molecular replacement with Phaser. Acta Crystallogr. D Biol. Crystallogr. *63*, 32–41.

McPherson, A., and Cudney, B. (2014). Optimization of crystallization conditions for biological macromolecules. Acta Crystallogr. F Struct. Biol. Commun. *70*, 1445–1467.

Micsonai, A., Wien, F., Kernya, L., Lee, Y.H., Goto, Y., Refregiers, M., and Kardos, J. (2015). Accurate secondary structure prediction and fold recognition for circular dichroism spectroscopy. Proc. Natl. Acad. Sci. U S A *112*, E3095–E3103.

Moon, A.F., Mueller, G.A., Zhong, X., and Pedersen, L.C. (2010). A synergistic approach to protein crystallization: combination of a fixed-arm carrier with surface entropy reduction. Protein Sci. *19*, 901–913.

Moore, B.W. (1965). A soluble protein characteristic of the nervous system. Biochem. Biophys. Res. Commun. *19*, 739–744.

Newman, J. (2005). Expanding screening space through the use of alternative reservoirs in vapor-diffusion experiments. Acta Crystallogr. D Biol. Crystallogr. *61*, 490–493.

Oh, Y.S., Gao, P., Lee, K.W., Ceglia, I., Seo, J.S., Zhang, X., Ahn, J.H., Chait, B.T., Patel, D.J., Kim, Y., and Greengard, P. (2013). SMARCA3, a chromatin-remodeling factor, is required for p11-dependent antidepressant action. Cell *152*, 831–843.

Okuda, M., and Nishimura, Y. (2014). Extended string binding mode of the phosphorylated transactivation domain of tumor suppressor p53. J. Am. Chem. Soc. *136*, 14143–14152.

Orre, L.M., Panizza, E., Kaminskyy, V.O., Vernet, E., Graslund, T., Zhivotovsky, B., and Lehtio, J. (2013). S100A4 interacts with p53 in the nucleus and promotes p53 degradation. Oncogene *32*, 5531–5540.

Raddum, A.M., Hollas, H., Shumilin, I.A., Henklein, P., Kretsinger, R., Fossen, T., and Vedeler, A. (2015). The native structure of annexin A2 peptides in hydrophilic environment determines their anti-angiogenic effects. Biochem. Pharmacol. *95*, 1–15.

Raj, N., and Attardi, L.D. (2017). The transactivation domains of the p53 protein. Cold Spring Harb. Perspect. Med. *7*, https://doi.org/10.1101/cshperspect.a026047.

Rajagopalan, S., Andreeva, A., Rutherford, T.J., and Fersht, A.R. (2010). Mapping the physical and functional interactions between the tumor suppressors p53 and BRCA2. Proc. Natl. Acad. Sci. U S A *107*, 8587–8592.

Rosenbaum, D.M., Cherezov, V., Hanson, M.A., Rasmussen, S.G., Thian, F.S., Kobilka, T.S., Choi, H.J., Yao, X.J., Weis, W.I., Stevens, R.C., and Kobilka, B.K. (2007). GPCR engineering yields high-resolution structural insights into beta2-adrenergic receptor function. Science *318*, 1266–1273.

Rosengarth, A., and Luecke, H. (2003). A calcium-driven conformational switch of the N-terminal and core domains of annexin A1. J. Mol. Biol. *326*, 1317–1325.

Rosengarth, A., and Luecke, H. (2004). Annexin A2. Does it induce membrane aggregation by a new multimeric state of the protein? Annexins *1*, e34–e41.

Rowell, J.P., Simpson, K.L., Stott, K., Watson, M., and Thomas, J.O. (2012). HMGB1-facilitated p53 DNA binding occurs via HMG-Box/p53 transactivation domain interaction, regulated by the acidic tail. Structure *20*, 2014–2024.

Shao, C., Zhang, F., Kemp, M.M., Linhardt, R.J., Waisman, D.M., Head, J.F., and Seaton, B.A. (2006). Crystallographic analysis of calcium-dependent heparin binding to annexin A2. J. Biol. Chem. *281*, 31689–31695.

Shen, W., Chen, D., Liu, S., Chen, L., Yu, A., Fu, H., and Sun, X. (2015). S100A4 interacts with mutant p53 and affects gastric cancer MKN1 cell autophagy and differentiation. Int. J. Oncol. *47*, 2123–2130.

Shin, J.S., Ha, J.H., Lee, D.H., Ryu, K.S., Bae, K.H., Park, B.C., Park, S.G., Yi, G.S., and Chi, S.W. (2015). Structural convergence of unstructured p53 family transactivation domains in MDM2 recognition. Cell Cycle *14*, 533–543.

Smith, D.B. (2000). Generating fusions to glutathione S-transferase for protein studies. Methods Enzymol. *326*, 254–270.

Smyth, D.R., Mrozkiewicz, M.K., McGrath, W.J., Listwan, P., and Kobe, B. (2003). Crystal structures of fusion proteins with large-affinity tags. Protein Sci. *12*, 1313–1322.

Stevens, R.C. (2000). Design of high-throughput methods of protein production for structural biology. Structure *8*, R177–R185.

Tamura, R., Oi, R., Akashi, S., Kaneko, M.K., Kato, Y., and Nogi, T. (2019). Application of the NZ-1 Fab as a crystallization chaperone for PA tag-inserted target proteins. Protein Sci. *28*, 823–836.

Tereshko, V., Uysal, S., Koide, A., Margalef, K., Koide, S., and Kossiakoff, A.A. (2008). Toward chaperone-assisted crystallography: protein engineering enhancement of crystal packing and X-ray phasing capabilities of a camelid single-domain antibody (VHH) scaffold. Protein Sci. *17*, 1175–1187.

Thorsen, T.S., Matt, R., Weis, W.I., and Kobilka, B.K. (2014). Modified T4 lysozyme fusion proteins facilitate G protein-coupled receptor crystallogenesis. Structure *22*, 1657–1664.

Tompa, P., and Fuxreiter, M. (2008). Fuzzy complexes: polymorphism and structural disorder in protein-protein interactions. Trends Biochem. Sci. *33*, 2–8.

Wang, Z.X. (1995). An exact mathematical expression for describing competitive binding of two different ligands to a protein molecule. FEBS Lett. *360*, 111–114.

Waugh, D.S. (2016). Crystal structures of MBP fusion proteins. Protein Sci. *25*, 559–571.

Yoon, M.K., Kim, B.Y., Lee, J.Y., Ha, J.H., Kim, S.A., Lee, D.H., Lee, M.S., Lee, M.K., Choi, J.S., Cho, J.H., et al. (2018). Cytoplasmic pro-apoptotic function of the tumor suppressor p73 is mediated through a modified mode of recognition of the anti-apoptotic regulator Bcl-XL. J. Biol. Chem. *293*, 19546–19558.

Please cite this article in press as: Ecsédi et al., Structure Determination of the Transactivation Domain of p53 in Complex with S100A4 Using Annexin A2 as a Crystallization Chaperone, Structure (2020), https://doi.org/10.1016/j.str.2020.05.001

STAR★METHODS

KEY RESOURCES TABLE

REAGENT or RESOURCE	SOURCE	IDENTIFIER
Bacterial and Virus Strains		
Bacteria: *E.coli* DH5α	NEB	#C2987I
Bacteria: *E.coli* BL21(DE3)	NEB	#C2527I
Chemicals, Peptides, and Recombinant Proteins		
P53 TAD^{1-60} peptide	This paper	P04637
P53 TAD^{17-56} peptide	This paper	P04637
P53 TAD^{17-56} peptide mutants	This paper	P04637
$ANXA2^{23-339}$	This paper	P07355
$ANXA2^{29-339}$	This paper	P07355
wtMBP	This lab	P0AEX9
P53 TAD^{17-56} – scS100A4Δ8 – $ANXA2^{29-339}$	This paper	N/A
scS100A4Δ8 – $ANXA2^{29-339}$	This paper	N/A
PDZ – $ANXA2^{23-339}$	This lab	N/A
wtMBP – scS100A4Δ8	This paper	N/A
wtMPB - PDZ	This lab	N/A
2nd PDZ domain of MAGI-1	This lab	Q96QZ7
scS100A4Δ8	This paper	N/A
S100A4	This lab	P26447
Tobacco etch virus (TEV) protease	This lab	Q0GDU8
5-(Iodoacetamido)-fluorescein	Sigma-Aldrich	#I9271
Isopropyl β-D-1-thiogalactopyranoside (IPTG)	Duchefa-Biochemie	#I1401
Tris(2-carboxyethyl)phosphine (TCEP)	Alfa Aesar	#040587
Phenylmethanesulfonyl fluoride (PMSF)	Sigma-Aldrich	#P7626
Morpheus screen	Molecular Dimensions	#MD1-47
JCSG+ screen	Molecular Dimensions	#MD1-37
Deposited Data		
Coordinates of p53 TAD^{17-56} – scS100A4Δ8 – $ANXA2^{29-339}$	This paper	PDB: 6T58
Coordinates of ANXA2	Rosengarth and Luecke, 2004	PDB: 1XJL
Coordinates of PKC phosphorylation-mimicking mutant (S26E) ANXA2	Ecsédi et al., 2017	PDB: 5LPX
Coordinates of Tyr24 phosphorylated ANXA2	Ecsédi et al., 2017	PDB: 5LQ0
Coordinates of ANXA2	Shao et al., 2006	PDB: 2HYW
Coordinates of bovine ANXA2	Raddum et al., 2015	PDB: 4X9P
Coordinates of Tyr24 phosphorylated ANXA2	Ecsédi et al., 2017	PDB: 5LQ2
Coordinates of MAGI-1 complexed with a RSK1 peptide	Gogl et al., 2018	PDB: 5N7D
Coordinates of ANXA2 complexed with S100A4	Ecsédi et al., 2017	PDB: 5LPU
Coordinates of S100A10 /Annexin A2 Heterotetramer	Oh et al., 2013	PDB: 4HRE
Coordinates of ANXA1	Rosengarth and Luecke, 2003	PDB: 1MCX
Coordinates of bovine ANXA6	Avila-Sakar et al., 1998	PDB: 1AVC
Oligonucleotides		
Oligonucleotides are presented in Table S1.		

(*Continued on next page*)

Continued

REAGENT or RESOURCE	SOURCE	IDENTIFIER
Recombinant DNA		
ANXA2$^{23-339}$ in modified pET15b vector (pANXA2$^{23-339}$)	This paper	Addgene ID: 136543 and 136546
ANXA2 $^{29-339}$ in modified pET15b vector (pANXA2$^{29-339}$)	This paper	Addgene ID: 136544 and 136545
wtMBP in in pET-MBP	This paper	N/A
P53 TAD$^{17-56}$ – scS100A4Δ8 – ANXA2$^{29-339}$ in modified pET15b vector (pANXA2$^{29-339}$)	This paper	N/A
scS100A4Δ8 – ANXA2$^{29-339}$ in modified pET15b vector (pANXA2$^{29-339}$)	This paper	N/A
PDZ – ANXA2$^{23-339}$ in modified pET15b vector (pANXA2$^{23-339}$)	Gogl et al., 2018	N/A
wtMBP – scS100A4Δ8 in pET-MBP	This paper	N/A
wtMPB – PDZ in pET-MBP	Gogl et al., 2018	N/A
PDZ in pET-MBP	Gogl et al., 2018	N/A
scS100A4Δ8 in modified pET15b vector (pEV)	This paper	N/A
S100A4 in modified pET15b vector (pEV)	Kiss et al., 2012	N/A
P53 TAD$^{1-60}$ in modified pGEX vector (pETARA)	This paper	N/A
P53 TAD$^{17-56}$ peptide in modified pGEX vector (pETARA)	This paper	N/A
P53 TAD$^{17-56}$ peptide mutants in modified pGEX vector (pETARA)	This paper	N/A
Tobacco etch virus (TEV) protease in pTH24 vector	van den Berg et al., 2006	N/A
Software and Algorithms		
Coot	Emsley et al., 2010	https://www2.mrc-lmb.cam.ac.uk/personal/
Phenix	Adams et al., 2010	https://www.phenix-online.org
Pymol	PYMOL	http://www.pymol.org
Phaser	McCoy, 2007	http://www-structmed.cimr.cam.ac.uk/phaser_obsolete/
XDS	Kabsch, 2010	http://xds.mpimf-heidelberg.mpg.de/
Origin for ITC 5.0	OriginLab	http://www.originlab.com/
Origin 8	OriginLab	http://www.originlab.com/
GeneTools	GeneTools	http://www.syngene.com/genetools-software-download
Bestsel	Micsonai et al., 2015	http://bestsel.elte.hu/
Other		
Phenyl Sepharose 6 Fast Flow	GE Healthcare	#17-0973-05
HiTrap SP HP cation exchange column	GE Healthcare	#17115101
Jupiter 300 C5 column	Phenomenex	#00G-4052-E0
384-well microplates	Corning	#3676
Profinity IMAC resin	Bio-Rad	#1560131
Protino Glutathione Agarose 4B resin	Macherey-Nagel	#745500.10
Amylose resin	NEB	#E8021S
HighTrap Heparin HP column	GE Healthcare (Sigma)	#GE17-0406-01
HiTrap Desalting column	GE Healthcare (Sigma)	#GE29-0486-84

RESOURCE AVAILABILITY

Lead Contact

Further information and requests for resources and reagents should be directed to and will be fulfilled by the Lead Contact, László Nyitray (nyitray@elte.hu)

Please cite this article in press as: Ecsédi et al., Structure Determination of the Transactivation Domain of p53 in Complex with S100A4 Using Annexin A2 as a Crystallization Chaperone, Structure (2020), https://doi.org/10.1016/j.str.2020.05.001

Materials Availability

Plasmids generated in this study have been deposited to Addgene (IDs of 136543, 136544, 136545 and 136546)

All unique/stable reagents generated in this study are available from the Lead Contact without restriction.

Data and Code Availability

Coordinates and structure factors have been deposited in the Protein Data Bank under accession code 6T58.

EXPERIMENTAL MODEL AND SUBJECT DETAILS

E. coli BL21(DE) Cells (NEB)

For protein expression. Cultures were grown in Luria-Bertani (LB) broth at 37°C.

E.coli DH5α Cells (NEB)

For cloning. Cultures were grown in Luria-Bertani (LB) broth at 37°C.

METHOD DETAILS

Cloning, Protein Expression and Purification

N-terminally truncated forms of human ANXA2 (23-339 and 29-339) (UniProt code: P07355), along with a short multi-cloning site, were cloned into a modified pET15 vector (pEV) that contains an N-terminal tobacco etch virus (TEV)-cleavable His_6-tag (pANXA2$^{23-339}$ and pANXA2$^{29-339}$). Human p53 TAD$^{1-60}$ and p53 TAD$^{17-56}$ (UniProt code: P04637) was cloned into a modified pGEX vector (pETARA) containing an N-terminal TEV-cleavable glutathione *S*-transferases (GST). QuikChange method was used to produce the p53 TAD$^{17-56}$ and the cys-p53 TAD$^{17-56}$ peptide mutants. The second PDZ domain of human Magi-1 protein (PDZ) (Uniprot code: Q96QZ7) was cloned previously by Gógl et. al. (Gogl et al., 2018). Single-chain human S100A4Δ8 (UniProt code: 26447) insert (consisting the two S100A4Δ8 subunit connected by a 6-residue-long GS-linker) was cloned into the pANXA2$^{29-339}$, pET-MBP and pEV vectors. In case of p53 TAD$^{17-56}$ – scS100A4Δ8 – ANXA2$^{29-339}$ construct, the p53 TAD$^{17-56}$ was cloned N-terminally to the scS100A4Δ8 in the scS100A4Δ8-pANXA2$^{29-339}$ construct with a 6-residue-long GS linker. The wild type S100A4, wtMBP-PDZ and ANXA2 proteins were previously cloned as described in: (Gogl et al., 2018; Ecsédi et al., 2017; Kiss et al., 2012).

WtMBP, wtMBP – PDZ, wtMBP – scS100A4Δ8, ANXA2$^{29-339}$, PDZ – ANXA2$^{23-339}$, scS100A4Δ8 – ANXA2$^{29-339}$, p53 TAD$^{17-56}$ – scS100A4Δ8 – ANXA2$^{29-339}$, scS100A4Δ8, PDZ and p53 TAD constructs were expressed in *E. coli* BL21(DE) cells. Transformed cultures were grown in Luria-Bertani (LB) broth supplemented with 100 μg/ml ampicillin at 37°C until the optical density at 600 nm reached 0.8. Expression was induced with 0.25 mM isopropyl β-D-1-thiogalactopyranoside (IPTG) at 18°C overnight or at 28°C for 4 hours in case of GST-fusions. Pelleted cells were disintegrated by ultrasonication in a buffer containing 20 mM Tris, pH 8, 300 mM NaCl, 0.1 mM tris(2-carboxyethyl)phosphine (TCEP), and 1 mM phenylmethanesulfonyl fluoride (PMSF). Cell lysates were clarified by centrifugation at 48,000 × g, and the supernatant was applied to Ni^{2+}-affinity chromatography column using Profinity IMAC resin (Bio-Rad) with 20 mM Tris, pH 8, 300 mM NaCl, 0.1 mM TCEP as wash buffer. His_6-tagged proteins were eluted with the wash buffer complemented with 250 mM imidazole. GST-fusions expressing cells were resuspended in a buffer containg 150 mM NaCl. After ultrasonication, the clarified cell lysates were loaded onto Protino Glutathione Agarose 4B resin (Macherey-Nagel). After thorough wash with the lysis buffer the GST-fusions were eluted using the washing buffer complemented with 10 mM reduced glutathione. GST and His_6-tag were eliminated using TEV (van den Berg et al., 2006) protease at room temperature overnight. Note that the His_6-tag was not removed from MBP-fusions. After complete cleavage, GST was removed from solution by heat denaturation followed by centrifugation. p53 fragments were further purified by reverse HPLC using a Jupiter 300 C5 column (Phenomenex). The p53 containing fractions were lyophilized and stored at -20°C. MBP, MBP – PDZ and MBP – scS100A4Δ8 constructs were further purified using MBP affinity purification (Amylose Resin, NEB) and eluted using 10 mM maltose in the washing buffer, than concentrated by Amicon Ultra-15 Centrifugal Filter Units and stored at -80°C. Following the removal of His_6-tag using reverse Ni^{2+}-affinity chromatography ANXA2$^{29-339}$, PDZ – ANXA2$^{23-339}$, scS100A4Δ8 – ANXA2$^{29-339}$ and p53 TAD$^{17-56}$ – scS100A4Δ8 – ANXA2$^{29-339}$ were dialyzed and separated by cation-exchange chromatography using HiTrap SP HP (GE Healthcare) column at pH 6.5. ScS100A4Δ8 – ANXA229-339 were also dialyzed in a 20 mM HEPES, pH 7.5, 150 mM NaCl, 1mM CaCl2 and 0.1 mM TCEP containing buffer and were applied to HighTrap Heparin HP (GE Healthcare) column and eluted using 10 mM EGTA containing washing buffer (Figure S1). ScS100A4Δ8 were applied to phenyl-Sepharose 6 resin column (GE Healthcare), washed with 20 mM HEPES, 50 mM NaCl, 0.5 mM $CaCl_2$, 0.1 mM TCEP, and eluted with the wash buffer supplemented with 5 mM EGTA. The recombinant proteins were concentrated using Amicon Ultra-15 Centrifugal Filter Units and stored at -80°C.

Fluorescent Labeling

Cys-p53 TAD$^{17-56}$ peptide was labeled selectively at the artificially cloned N-terminal Cys residue with a 3-fold excess of 5-(iodoacetamido)-fluorescein (5-IAF, Sigma-Aldrich) in 20 mM Hepes pH 7.5, 150 mM NaCl, 1 mM TCEP buffer incubating the samples for 18 hours in the dark at 4°C. The fluorescein-conjugated p53 TAD$^{17-56}$ (referred as Fl-p53 TAD) was separated from the non-reacted dye and unconjugated peptide by gel filtration (HiTrap Desalting columns, GE) and RP-HPLC using Jupiter 300 C5 column (Phenomenex).

Crystallization, Data Collection and Structure Determination

Crystallization samples contained 350 μM p53 TAD$^{17-56}$ – scS100A4Δ8 – ANXA2$^{29-339}$, 20 mM HEPES pH 7.5, 100 mM NaCl, 1mM TCEP and 5 mM $CaCl_2$ before mixing. Crystallization was carried out in standard hanging drop vapor-diffusion set-up at 20°C, mixing the protein and the precipitant solution in different volumes using distinct protein to precipitant ratios. 1.25 M NaCl was used (Newman, 2005) as reservoir solution. Best crystals grew in the D6 condition of Morpheus screen (Molecular dimension). Crystals were supplemented with 20% glycerol before flash cooling in liquid nitrogen. Data were collected on the PXIII beamline of the Swiss Light Source (Villigen) at 100 K with a wavelength of 1 Å (Table 1). Data were processed with XDS (Kabsch, 2010). The phase problem was solved by molecular replacement (MR) in PHASER (McCoy, 2007) with a high resolution structure of S100A4 (Gingras et al., 2008) and ANXA2 (Ecsédi et al., 2017) as search models. Structure refinement was carried out in PHENIX (Adams et al., 2010) and structure remodelling/building was done in Coot (Emsley et al., 2010). Crystal structure was deposited to the Protein Data Bank under the accession code of 6T58.

Crystal Screening of Chimera Constructs

WtMBP, wtMBP – PDZ and wtMBP – scS100A4Δ8 constructs were used in 2 mM (at first in 250 μM), while ANXA2$^{29-339}$, PDZ – ANXA2$^{23-339}$, scS100A4Δ8 – ANXA2$^{29-339}$, scS100A4Δ8 and PDZ were used in 250 μM concentration in 20 mM HEPES pH 7.5, 100 mM NaCl, 1mM TCEP and 5 mM $CaCl_2$ containing buffer before mixing. Samples were dialyzed together before experiments. Note that, Ca^{2+} containing protein solutions may form salt crystals, thus false positive results with some conditions of crystallization screens (especially with phosphates and sulphates) might appear. By dialyzing all samples together in the same Ca^{2+} containing buffer, the chances for such false hits are supposed to be similar everywhere, thus the results of different constructs could be compared directly. The plates were analyzed by two independent crystallographers to find crystals. When crystals were observed, we performed careful morphology analysis under polarized light and if it was necessary, we used IZIT crystal dye to stain protein crystals or we performed diffraction test measurements on an in-house diffractometer to make sure about their protein composition. Crystallization was done in standard hanging drop vapor-diffusion set-up at 20°C, either using a crystallization robot (LCP Mosquito) or by hand mixing the protein and the precipitant solutions of JCSG+ and Morpheus screens (Molecular Dimensions) in equal protein/precipitant volume. Crystals appearing in both methods were only accepted and showed in this paper. In case of screening experiments the reservoir solutions were identical to the precipitant while 1.25 M NaCl was used (Newman, 2005) when the concentration dependence of crystallogenesis was studied. Crystal formation was monitored for a week in the former and for a month in the latter case.

Isothermal Titration Calorimetry (ITC)

60 μM wild type S100A4 dimer was titrated with p53 TAD$^{1-60}$ peptide (500 μM) at 37°C in 20 mM HEPES pH 7.5, 150 mM NaCl, 1 mM $CaCl_2$, and 1 mM TCEP containing buffer using a MicroCal VP-ITC instrument. The injection volume was 5 - 5 μL with 400 s time intervals between injections. The Origin for ITC 5.0 (OriginLab) software package was used for data processing, and the model "One Set of Sites" was fitted.

Circular Dichroism (CD) Spectrometry

Far UV CD spectra of 50 μM p53 TAD$^{1-60}$ and 80 μM wild type S100A4 dimer alone and together were measured in 20 mM HEPES pH 7.5, 20 mM NaCl, 1 mM $CaCl_2$, and 1 mM TCEP containing buffer at 25°C using a 0.01 cm quartz cuvette (Hellma) in a Jasco J-715 spectropolarimeter. We assumed that the secondary structure of S100A4 does not change upon p53 binding (Kiss et al., 2012), thus the spectra of the bound p53 fragment was produced as the difference between the spectrum of S100A4 - p53 TAD$^{1-60}$ complex and of S100A4 alone. CD spectra of apo and S100A4 bound p53 TAD$^{1-60}$ were analyzed using BeStSel method (Micsonai et al., 2015). To ensure that the buffer does not contribute to the CD spectrum of apo and complexed p53 TAD$^{1-60}$, corrections with the CD spectrums of the blank buffer or the free S100A4 (also includes the CD spectrum of the buffer) were applied respectively.

Fluorescence Polarization (FP) Measurements

Measurements were carried out using 20 mM HEPES pH 7.5, 150 mM NaCl, 1 mM $CaCl_2$, 0.1 mM TCEP and 0.05% Tween-20 containing buffer. Fluorescence polarization was measured in 384-well plates (Corning) using Synergy H4 multi-mode microplate reader (BioTek). Firstly, the binding affinity of S100A4 to Fl-p53 TAD$^{17-56}$ (50 nM) was determined in a direct binding assay. The quadratic binding equation was used for fitting to data. Based on the result of the direct FP measurement 50 nM Fl-p53 TAD$^{17-56}$ complexed with 2.5 μM wild type S100A4 dimer was titrated with unlabeled wild type p53$^{1-60}$, p53$^{17-56}$ and mutated p53$^{17-56}$ peptides (competitive FP measurements). The competitive binding equation (Wang, 1995) was used for fitting to data. Origin 8 was used for data evaluation. Measurements were carried out in triplicates.

QUANTIFICATION AND STATISTICAL ANALYSIS

Percentages were calculated in Figure 4 and in the Results sections of "*In vitro* characterization of the p53 TAD – S100A4 complex" and "Comparing the crystal forming ability of ANXA2 and wtMBP".

K_d values were calculated, using competitive binding equation in Figures 1D and 3B. The detailed descriptions are in figure labels and STAR Methods section. Each data point represents the mean ± SD of three independent experiments. Origin 8 software was used.